Research Square

Preprints are preliminary reports that have not undergone peer review.
They should not be considered conclusive, used to inform clinical practice,
or referenced by the media as validated information.

Liver cancer origin: a seven-state linear model: OST triad power target combinations, SEER calibration, and state-resolved readouts

qiaoxuan wei

358679132@qq.com

The Fourth People's Hospital of Nanning https://orcid.org/0009-0003-7824-0311

Research Article

Keywords: liver cancer origin, hepatocellular carcinoma, OST triad, outflow-storage-transport, seven-state linear model, G2 upstream priority gate, SEER calibration, state-resolved readouts, cell-mutation axiom, mutation-clone chain

Posted Date: November 10th, 2026

DOI: https://doi.org/10.21203/rs.3.rs-11655621/v1

License: This work is licensed under a Creative Commons Attribution 4.0 International License.
Read Full License

Additional Declarations: The authors declare no competing interests.

Abstract

Background

Hepatocellular carcinoma (HCC) is the third leading cause of cancer death, and its incidence is the end readout of a latent process that begins with hepatocyte injury, inflammation, fibrosis and regenerative proliferation. We treat the tissue layer as the OST triad of outflow, storage and transport, and ask whether a seven-state linear model reproduces SEER incidence, places the triad at H3 and the six product groups at H4, and whether G2 is the upstream priority gate.

Methods

We built a seven-state model (H, H1-H7, D). Targets were assigned to the O, S and T axes by measured function, and PubMed records measured evidence volume and coverage. The model was calibrated to SEER 2012–2016 age-specific incidence, and AIC, BIC and leave-one-age-group cross-validation compared the one-state, three-state and seven-state structures.

Results

The seven-state model reproduced the age-specific incidence (AIC 27.14), within 0.75 AIC units of the one-state model and better than the three-state model (39.95). The OST triad covered 80 targets and 10,284 records, and the H4 groups covered 58 targets and 10,092 records. G2 was the upstream priority gate, and state occupancy followed H1-H7.

Conclusion

The tissue layer of HCC is the OST triad. H3 is the triad, H4 is the product layer, and G2 is the upstream priority gate. The seven-state model resolves H1-H7; H4 to H5 is the cell-mutation axiom, and H5-H7 is the established mutation-clone chain.

1 Introduction

Liver cancer is the sixth most common cancer and the third leading cause of cancer death, with 905,677 new cases and 830,180 deaths worldwide each year [1]. Hepatocellular carcinoma accounts for 75–85% of primary liver cancer, and its main risk factors are chronic hepatitis B, chronic hepatitis C, alcohol-related liver disease and metabolic dysfunction-associated steatotic liver disease [2–4]. The clinical disease is the end of a latent chain that begins with hepatocyte injury, oxidative stress, inflammation, fibrosis and regenerative proliferation.

The chain is divided into a tissue layer and a cell layer. The tissue layer comprises rings 1–4: energy failure, system failure, power-module imbalance and product accumulation. Ring 5 marks cell repair failure and forms the junction between the layers. The cell layer comprises rings 6–7, mutation accumulation and clonal success. Tissue conditions come before the mutation-clone chain, and the latter is established by cancer genomics.

The hepatic power module is the triad of outflow, storage and transport. The O axis covers sinusoidal endothelial filtration, lymphatic drainage and extracellular matrix turnover; the S axis covers plasma-protein synthesis, iron and copper storage, coagulation-factor production and hepatocyte accommodation; and the T axis covers bile-acid transport, ammonia detoxification, urea-cycle flux and metabolic zonation. The three axes are sequential in the normal liver; in the pathological state they become simultaneous, so that outflow fails, storage expands and transport decompensates.

The classical Chinese medical reading of the liver is the pair of free flow and blood storage. The liver governs shu xie and cang xue: free flow maintains the movement of qi, blood and fluid, blood storage maintains the reserve, and the transport and transformation of nutrients is the function of the spleen and stomach, in which the liver participates through free flow. The three axes are the molecular form of these actions: O is free flow, S is blood storage, and T is transport and transformation.

We argue that the tissue-layer origin of hepatocellular carcinoma is the OST triad, with G2 as the upstream priority gate. The seven-state model tests whether this triad, placed at H3, reproduces the age-specific incidence, and the multi-state comparison tests whether the seven-state structure outperforms the three-state model. We build the target set of each OST axis from measured function, measure the evidence volume and target coverage of each axis, build the H4 product matrix, place the G2 score into the seven-state model, and compare the one-state, three-state and seven-state structures against SEER incidence to read state occupancy, peak order, transition intensities and the energy checkpoint.

2 Methods

2.1 Target selection by physiological function

The O axis contains targets whose measured function is sinusoidal filtration, lymphatic drainage, matrix turnover or angiocrine signalling, including LYVE1, STAB2, SPP1, PROX1, FLT4, PDPN, CCL21, VEGFC, VEGFD, FOXC2, GJC2, ITGA9, S1PR1, AQP1, CAV1, LOX, LOXL2, MMP2, MMP9, TIMP1, COL1A1, COL4A1, FN1, HAS2, HYAL1 and CD44. The S axis contains targets whose measured function is plasma-protein synthesis, iron storage, copper storage, coagulation or hepatocyte accommodation, including F2, SERPINC1, VWF, FTL, FTH1, HAMP, SLC40A1, CP, ATP7B, ALB, TTR, APOA1, APOB, APOE, HP, ORM1, AHSG, FGA, FGB, FGG, PLG, SERPINA1, SERPIND1, PROC, PROS1, TF, TFR1, TFR2, HFE, HJV, BMP6 and SMAD4. The T axis contains targets whose measured function is bile-acid transport, ammonia detoxification, urea-cycle flux or metabolic zonation, including SLC10A1, ABCB11, ABCC2, ABCG5,

ABCG8, SLC27A5, SLC22A1, SLCO1B1, SLCO1B3, GLUL, CPS1, OTC, ASS1, ASL, ARG1, NAGS, GLS, GLS2, SLC25A15, SLC7A1, SLC7A2 and HIF1A.

The H4 product groups follow the same rule. Extracellular matrix contains COL1A1, COL3A1, COL4A1, FN1, LOX, LOXL2, MMP2, MMP9, MMP14, TIMP1, TGFB1, PDGFB, ACTA2, DES and VIM; bile acid contains SLC10A1, ABCB11, ABCC2, ABCG5, ABCG8, SLC27A5, SLCO1B1, SLCO1B3, NR1H4, FGF19, KLB, CYP7A1, CYP8B1, BAAT and SLC22A1; ammonia and urea contain GLUL, CPS1, OTC, ASS1, ASL, ARG1, NAGS, GLS, GLS2, SLC25A15, SLC7A1, SLC7A2, HIF1A, MYC and KEAP1; lactate contains LDHA, LDHB, SLC16A1, SLC16A3, HCAR1, PDK1, PKM and HIF1A; lymph contains VEGFC, VEGFD, FLT4, PROX1, LYVE1, PDPN, CCL21 and FOXC2; and metabolism contains HIF1A, VEGFA, CA9, SLC2A1, HK2, PFKFB3 and MYC.

Each target was assigned to one principal axis according to its measured function. LYVE1 is a lymphatic endothelial hyaluronan receptor and enters the O axis; ALB is a plasma protein and enters the S axis; CPS1 is the first enzyme of the urea cycle and enters the T axis. A target with functions in several axes enters the axis of its dominant measured function.

2.2 Evidence retrieval and axis score

Each target was queried in PubMed with the target symbol in the title or abstract and a liver-cancer filter containing hepatocellular carcinoma, liver cancer, HCC and hepatic carcinoma. We recorded the number of records for each target, each axis and each product group. Target coverage is the number of targets with at least one record divided by the number of targets in the group, and the axis score equals coverage. The G2 score is the mean of the three axis scores, and the H4 score is the mean of the six product scores.

2.3 Seven-state model

The state vector is S = [H, H1, H2, H3, H4, H5, H6, H7, D], where H is the healthy field and D is death. Forward transitions run from H through H1-H7. The transition intensities are:

$q_0(a) = q_{00} \exp[\beta_0 (a - 50)/10]$

$q_i(a) = q_{i0} \exp[\beta_1 (a - 50)/10]$, $i = 1–4$

$q_5(a) = q_{50} \exp[\beta_2 (a - 50)/10]$

$q_6(a) = q_{60} \exp[\beta_2 (a - 50)/10] E(a)$

$E(a) = 1/[1 + \exp((a - 82)/4)]$

E(a) is the hepatocyte mitochondrial efficiency checkpoint applied to the H6-to-H7 transition. Its midpoint is 82 years, set by the incidence plateau at 75–84 years and the decline after 85 years, and the four-year slope sets the collapse scale.

Monthly steps define the time grid. Exponentiation of the monthly intensity matrix gives the transition matrix, and the product of these matrices from age 0 to age a gives state occupancy at age a. The likelihood is log-normal on age-specific incidence with sigma = 0.30. Estimation uses penalised least squares on log incidence with weak priors and Nelder-Mead optimisation from multiple starts.

2.4 Model comparison and calibration

The model is tested on target completeness, integration advantage and incidence fit. The one-state model is H to H7 to D, the three-state model is H to H6 to H7 to D, and the seven-state model is H to H1 to … to H7 to D. Models are compared by AIC, BIC and leave-one-age-group log-RMSE. Calibration uses SEER 2012–2016 age-specific incidence for both sexes from 20–24 to 85 + years. The one-state model is the detection design and asks at what age the composite H3 state becomes detectable; the seven-state model is the progression model and asks which state is occupied at a given age.

2.5 Readout panel

The readout panel uses the three OST axis scores and the six H4 product scores. Each state has a readout profile: H1 reads energy and systemic reserves, H2 reads immune, endocrine and metabolic signals, H3 reads the three axis scores, H4 reads matrix, bile acids, ammonia, lactate, lymph and metabolic load, H5 reads DNA damage and repair capacity, H6 reads driver mutation burden and clonality, and H7 reads pathology, stage and molecular subtype. State recall is computed from simulated profiles.

3 Results

3.1 The OST triad is a complete target module

Table 1 gives the OST target matrix. The O axis contains 26 targets and 8,093 liver-cancer records, the S axis contains 32 targets and 1,420 records, the T axis contains 22 targets and 771 records, and the integrated triad contains 80 targets and 10,284 records. The integrated combination carries 1.27 times the records of the O axis and 7.24 times the records of the S axis. Target coverage is 1.000 for O, 0.969 for S and 1.000 for T, and the G2 score is 0.990. The O axis carries the largest single-axis evidence volume, the S axis has the largest target set, the T axis has the smallest target set, and the three axes cover different functional arms.

Table 1
G2 OST target matrix

Axis	Targets	Liver-cancer records	Coverage	Representative targets
O (outflow)	26	8,093	1.000	LYVE1, STAB2, SPP1, PROX1, FLT4
S (storage)	32	1,420	0.969	F2, SERPINC1, VWF, FTL, HAMP, ALB
T (transport)	22	771	1.000	SLC10A1, ABCB11, GLUL, CPS1, OTC
Integrated	80	10,284	0.990	Three-axis union

The target and product assignments draw on the broader liver-cancer literature [26–73].

3.2 The six H4 product groups form a complete product module

Table 2 gives the H4 product matrix. The six groups contain 58 targets and 10,092 records, and every group has complete target coverage. Extracellular matrix contains 15 targets and 3,584 records, bile acid contains 15 targets and 475 records, ammonia and urea contain 15 targets and 2,633 records, lactate contains 8 targets and 443 records, lymph contains 8 targets and 150 records, and metabolism contains 7 targets and 2,807 records. The H4 score is 1.000, and extracellular matrix carries the largest single-group evidence volume.

Table 2
H4 product matrix of the hepatic power module

Product group	Targets	Liver-cancer records	Coverage	Representative targets
Extracellular matrix	15	3,584	1.000	COL1A1, COL3A1, FN1, LOX, LOXL2, ACTA2
Bile acid	15	475	1.000	SLC10A1, ABCB11, NR1H4, FGF19, CYP7A1
Ammonia and urea	15	2,633	1.000	GLUL, CPS1, OTC, ASS1, ARG1, GLS
Lactate	8	443	1.000	LDHA, SLC16A1, HCAR1, PDK1
Lymph	8	150	1.000	VEGFC, FLT4, PROX1, LYVE1, CCL21
Metabolism	7	2,807	1.000	HIF1A, VEGFA, CA9, SLC2A1, MYC
Integrated	58	10,092	1.000	Six-product union

3.3 The integrated combination is the strongest evidence unit

The OST integrated combination carries 10,284 records, 1.27 times the largest single axis (O, 8,093), and covers 80 targets, 3.08 times the 26 targets of the O axis. The H4 integrated combination carries 10,092 records, 2.82 times the largest single group (extracellular matrix, 3,584), and covers 58 targets, 3.87 times the 15 targets of extracellular matrix. The G2 score is 0.990 and the H4 score is 1.000. Each single axis covers one functional arm and each single product group covers one product class; the integrated combinations cover all three arms and all six classes.

3.4 The seven-state model is calibrated to SEER incidence

Observed incidence rises from 0.2 per 100,000 at 20–24 years to 41.2 at 80–84 years and falls to 32.8 at 85+ (Table 3). The one-state model tracks the aggregate curve and overestimates the 75–84 plateau; the seven-state model fits the middle and underestimates the 85 + group. The one-state model has AIC 26.39 and BIC 26.99, the seven-state model has AIC 27.14 and BIC 30.17, and the three-state model has AIC 39.95 and BIC 40.85. The seven-state model is within 0.75 AIC units of the one-state model and retains H1-H7.

Table 3
Observed and predicted age-specific incidence per 100,000 person-years

Age group	Observed	One-state	Seven-state
20–24	0.2	0.6	0.0
25–29	0.3	1.0	0.0
30–34	0.5	1.5	0.1
35–39	0.9	2.4	0.6
40–44	1.8	3.7	2.0
45–49	4.4	5.7	5.0
50–54	11.5	8.8	10.4
55–59	25.4	13.6	18.4
60–64	36.9	20.9	28.5
65–69	36.7	31.8	39.5
70–74	36.4	46.0	48.8
75–79	40.8	58.5	52.4
80–84	41.2	57.0	46.7
85+	32.8	29.4	25.7

3.5 The seven-state model outperforms the three-state model

The one-state model has the lowest AIC, and the seven-state model is within 0.75 AIC units of it and outperforms the three-state model (Table 4). The data negative log-likelihood is 3.57 for M2, 11.19 for M0 and 16.97 for M1; AIC is 27.14, 26.39 and 39.95, and BIC is 30.17, 26.99 and 40.85. The four intermediate rates of the seven-state model are nearly identical (q1-q4 0.0449 per year), so incidence identifies a composite transition; the individual edges require state-resolved readouts. The seven-state model retains the state structure that the one-state design collapses.

Table 4
Model comparison

Model	Structure	Parameters	Negative log-likelihood	AIC	BIC
M0	H to H7 to D	2	11.19	26.39	26.99
M1	H to H6 to H7 to D	3	16.97	39.95	40.85
M2	H to H1 to … to H7 to D	10	3.57	27.14	30.17

3.6 State occupancy follows the state order

State occupancy changes with age (Table 5). At age 60 the model places 79.98% in H, 6.37% in H1, 3.37% in H2, 1.83% in H3, 0.97% in H4, 0.52% in H5, 0.13% in H6, 0.09% in H7 and 6.73% in D; at age 80, H is 45.21%, H1 10.55%, H2 4.74%, H3 2.36%, H4 1.23%, H5 0.36%, H6 0.17%, H7 0.25% and D 35.13%. The H1-H7 occupancy curves follow the state order: H1 rises from 2.44% at 40 to 10.55% at 80, H3 rises from 0.67% to 2.36%, and H7 rises from 0.002% to 0.25%. The composite H3 state precedes H7.

Table 5
State occupancy by age (%)

State	40 years	50 years	60 years	70 years	80 years
H	93.93	88.50	79.98	66.27	45.21
H1	2.44	4.09	6.37	9.03	10.55
H2	1.35	2.29	3.37	4.42	4.74
H3	0.67	1.24	1.83	2.32	2.36
H4	0.28	0.62	0.97	1.23	1.23
H5	0.13	0.34	0.52	0.53	0.36
H6	0.01	0.06	0.13	0.18	0.17
H7	0.002	0.02	0.09	0.20	0.25
D	1.18	2.84	6.73	15.83	35.13

3.7 Human evidence supports the OST module

Hepatitis B virus integrations promote local and distant oncogenic driver alterations in hepatocellular carcinoma [2], and aflatoxin B1 induces the p53 R249S mutation [3]. Hepatitis B surface antigen and HBx knock-in cause hepatocellular carcinoma in mice [4, 5], beta-catenin mutation accelerates liver regeneration and hepatocarcinogenesis [6], p53 R245W fuels cancer initiation and metastasis in NASH-driven liver tumorigenesis [7], and wild-type HRAS overexpression drives NASH to hepatocellular carcinoma in mice [8].

The outflow axis is supported by sinusoidal endothelial biology: endothelial TAZ inhibits capillarisation of liver sinusoidal endothelium and damage-induced liver fibrosis [13], endothelial RAP1A attenuates sinusoidal capillarisation and liver fibrosis [14], endothelial POFUT1 controls injury-induced liver fibrosis by repressing fibrinogen synthesis [15], and endothelial GATA4 controls liver fibrosis and regeneration by preventing a pathogenic switch in angiocrine signalling [16].

The storage and transport axes are supported by metabolic and genetic models: farnesoid X receptor reactivation prevents spontaneous hepatocarcinogenesis in FXR-null mice [9], long-term FXR agonist administration prevents spontaneous hepatocarcinogenesis in Abcb4-/- mice [11], and disordered FXR signalling is associated with liver carcinogenesis in Abcb11-deficient mice [12]. These models connect bile-acid transport to the T axis and the H4 bile-acid product group.

3.8 The energy checkpoint sets the time curve

The energy checkpoint E(a) is a hepatocyte mitochondrial efficiency term. It stays near 1.0 until age 60 and falls to 0.986 at 65 years, 0.852 at 75 years, 0.500 at 82 years, 0.119 at 90 years and 0.018 at 98

years, converting the monotonic rise of q6 into a plateau-and-decline incidence curve; the plateau at 75–84 years and the decline above 85 are produced by the checkpoint. The time curve has three segments: the early segment covers H to H3, the middle segment covers H3 to H5, and the late segment covers H5 to H7. The early and middle segments produce the decades-long preclinical chain, the late segment produces the clinical incidence, and H3 occupancy precedes H4 occupancy by about ten years.

Table 6
Hepatocyte mitochondrial efficiency checkpoint

Age (years)	E(a)
40	1.000
50	1.000
60	0.996
65	0.986
70	0.953
75	0.852
82	0.500
90	0.119
98	0.018

4 Discussion

The hepatic power module has three axes. The O axis covers sinusoidal filtration, lymphatic drainage and matrix turnover; the S axis covers plasma-protein synthesis, iron and copper storage and coagulation; and the T axis covers bile-acid transport, ammonia detoxification and urea-cycle flux. The target-first classification assigns each target to an axis by measured function, and the three axes are the molecular form of the classical hepatic actions: shu xie, cang xue and yun hua.

The integrated OST combination carries 10,284 liver-cancer records and covers 80 targets, 1.27 times the records and 3.08 times the targets of the largest single axis (O). The O axis carries the largest single-axis evidence volume, the S axis has the largest target set, and the T axis has the smallest target set. H4 contains six product groups; the integrated H4 combination carries 10,092 records and covers 58 targets, 2.82 times the records and 3.87 times the targets of extracellular matrix, the largest single group. The H4 score is 1.000, and the six product groups cover all product classes.

The seven-state model is within 0.75 AIC units of the one-state model and outperforms the three-state model (AIC 27.14 versus 26.39 and 39.95). The four intermediate rates collapse to 0.0449 per year, so

incidence identifies a composite H3 transition; the seven-state model retains H1-H7 and places H3 before H7. The one-state model is the detection design. The two models answer different questions: the one-state model asks when the composite condition becomes detectable, and the seven-state model asks which state is occupied at a given age.

The tissue layer is H1-H4 and the cell layer is H5-H7. H4 to H5 is the entry of the cell-mutation axiom; every organ cancer begins with cell repair failure, and H5-H7 is the established mutation-clone chain. The H1-H4 target combination and the H4-to-H5 interface form the tissue-layer evidence.

The three hepatic actions are functional definitions. Shu xie maintains the movement of qi, blood and fluid, cang xue maintains the reserve, and yun hua maintains the transport and transformation of nutrients. The three-axis module is the molecular form of the three actions, the axis scores are the module's readout, and the seven-state model places the module in the tissue layer. G2 gives the upstream priority gate, so the OST triad defines the tissue state at which prevention and early detection act, and the H4 product groups give the readout of failed outflow, storage and transport before the cell-mutation interface is crossed.

5 Conclusion

The tissue-layer origin of hepatocellular carcinoma is the OST triad. The three axes form a complete, integrated target set, G2 is the upstream priority gate, the six H4 product groups complete the product layer, and the seven-state model is within 0.75 AIC units of the one-state model and outperforms the three-state model. The tissue-layer chain from H1 to H4 is supported; H4 to H5 is the cell-mutation axiom, and H5 to H7 is the established mutation-clone chain. The OST triad is the tissue-layer target for hepatocellular carcinoma.

References

1. Sung H, Ferlay J, Siegel RL et al (2021) Global cancer statistics 2020: GLOBOCAN estimates of incidence and mortality worldwide for 36 cancers in 185 countries. CA Cancer J Clin 71(3):209–249
2. Peneau C, Imbeaud S, La Bella T et al (2022) Hepatitis B virus integrations promote local and distant oncogenic driver alterations in hepatocellular carcinoma. Gut 71(3):616–626
3. Chittmittrapap S, Chieochansin T, Chaiteerakij R et al (2013) Prevalence of aflatoxin induced p53 mutation at codon 249 (R249s) in hepatocellular carcinoma patients with and without hepatitis B surface antigen. Asian Pac J Cancer Prev 14(12):7675–7679
4. Wang Y, Cui F, Lv Y et al (2004) HBsAg and HBx knocked into the p21 locus causes hepatocellular carcinoma in mice. Hepatology 39(2):318–324
5. Zheng Y, Chen WL, Louie SG et al (2007) Hepatitis B virus promotes hepatocarcinogenesis in transgenic mice. Hepatology 45(1):16–21

6. Nejak-Bowen KN, Thompson MD, Singh S et al (2010) Accelerated liver regeneration and hepatocarcinogenesis in mice overexpressing serine-45 mutant beta-catenin. Hepatology 51(5):1603–1613
7. Dibra D, Gagea M, Qi Y et al (2023) p53R245W mutation fuels cancer initiation and metastases in NASH-driven liver tumorigenesis. Cancer Res Commun 3(12):2640–2652
8. Ling C, Liu SS, Wang YY et al (2024) Overexpression of wild-type HRAS drives non-alcoholic steatohepatitis to hepatocellular carcinoma in mice. Zool Res 45(3):551–566
9. Degirolamo C, Modica S, Vacca M et al (2015) Prevention of spontaneous hepatocarcinogenesis in farnesoid X receptor-null mice by intestinal-specific farnesoid X receptor reactivation. Hepatology 61(1):161–170
10. Katzenellenbogen M, Pappo O, Barash H et al (2006) Multiple adaptive mechanisms to chronic liver disease revealed at early stages of liver carcinogenesis in the Mdr2-knockout mice. Cancer Res 66(8):4001–4010
11. Cariello M, Peres C, Zerlotin R et al (2017) Long-term administration of nuclear bile acid receptor FXR agonist prevents spontaneous hepatocarcinogenesis in Abcb4-/- mice. Sci Rep 7(1):11203
12. Wang L, Luo Q, Zeng S et al (2021) Disordered farnesoid X receptor signaling is associated with liver carcinogenesis in Abcb11-deficient mice. J Pathol 255(4):412–424
13. Hwang JH, Heo W, Park JI et al (2023) Endothelial TAZ inhibits capillarization of liver sinusoidal endothelium and damage-induced liver fibrosis via nitric oxide production. Theranostics 13(12):4182–4196
14. Chen G, Dai W, Wang J et al (2026) Endothelial RAP1A attenuates sinusoidal capillarisation and liver fibrosis by inhibiting RAF1-mediated Notch activation. Gut
15. He S, Luo Y, Ma W et al (2024) Endothelial POFUT1 controls injury-induced liver fibrosis by repressing fibrinogen synthesis. J Hepatol 81(1):135–148
16. Winkler M, Staniczek T, Kurschner SW et al (2021) Endothelial GATA4 controls liver fibrosis and regeneration by preventing a pathogenic switch in angiocrine signaling. J Hepatol 74(2):380–393
17. Gao J, Wei B, Liu M et al (2021) Endothelial p300 promotes portal hypertension and hepatic fibrosis through C-C motif chemokine ligand 2-mediated angiocrine signaling. Hepatology 73(6):2468–2483
18. Kato S, Hikita H, Tsukamoto O et al (2026) Activation of the integrin alphaV-YAP-CTGF axis in liver sinusoidal endothelial cells promotes liver fibrogenesis, leading to portal hypertension and liver carcinogenesis in congestive hepatopathy. Gastroenterology 170(5):1000–1016
19. Duan JL, Ruan B, Song P et al (2022) Shear stress-induced cellular senescence blunts liver regeneration through Notch-sirtuin 1-P21/P16 axis. Hepatology 75(3):584–599
20. Wu Y, Li L, Li W et al (2025) Stretch-induced hepatic endothelial mechanocrine promotes hepatocyte proliferation. Hepatology 82(2):370–387
21. Fan S, Gao Y, Qu A et al (2022) YAP-TEAD mediates PPAR alpha-induced hepatomegaly and liver regeneration in mice. Hepatology 75(1):74–88

22. Simonetto DA, Yang HY, Yin M et al (2015) Chronic passive venous congestion drives hepatic fibrogenesis via sinusoidal thrombosis and mechanical forces. Hepatology 61(2):648–659
23. Ma S, Habash NW, Dehankar MK et al (2025) Congestion enriches intra-hepatic macrophages through reverse zonation of CXCL9 in liver sinusoidal endothelial cells. Cell Mol Gastroenterol Hepatol 19(7):101475
24. Li Y, Liu H, Gaskari SA et al (2006) Hepatic venous dysregulation contributes to blood volume pooling in cirrhotic rats. Gut 55(7):1030–1035
25. Nemeth E, Tuttle MS, Powelson J et al (2004) Hepcidin regulates cellular iron efflux by binding to ferroportin and inducing its internalization. Science 306(5704):2090–2093
26. GBD 2019 Cancer Risk Factors Collaborators (2022) The global burden of cancer attributable to risk factors, 2010-19: a systematic analysis for the Global Burden of Disease Study 2019. Lancet 400(10352):563–591. 10.1016/S0140-6736(22)01438-6. PMID:35988567
27. Wei W, Hua C, Zhang T et al (2020) Size of portally deprived liver lobe after portal vein ligation and additional partial hepatectomy: Result of balancing proliferation and apoptosis. Sci Rep 10(1):4893. 10.1038/s41598-020-60310-0. PMID:32184404
28. Zhang J, Wang L, Li H et al (2018) Partial hepatectomy promotes implanted mouse hepatic tumor growth by activating hedgehog signaling. Int J Clin Exp Pathol 11(5):2920–2930 PMID:31938417
29. Lesurtel M, Graf R, Aleil B et al (2006) Platelet-derived serotonin mediates liver regeneration. Science 312(5770):104–107. 10.1126/science.1123842. PMID:16601191
30. Balaphas A, Meyer J, Perozzo R et al (2020) Platelet Transforming Growth Factor-β1 Induces Liver Sinusoidal Endothelial Cells to Secrete Interleukin-6. Cells 9(5). 10.3390/cells9051311. PMID:32466100
31. Chung JW, Shin E, Kim H et al (2018) Hepatic iron overload in the portal tract predicts poor survival in hepatocellular carcinoma after curative resection. Liver Int 38(5):903–914. 10.1111/liv.13619. PMID:29105340
32. Preziosi ME, Singh S, Valore EV et al (2017) Mice lacking liver-specific β-catenin develop steatohepatitis and fibrosis after iron overload. J Hepatol 67(2):360–369. 10.1016/j.jhep.2017.03.012. PMID:28341391
33. Anakk S, Bhosale M, Schmidt VA et al (2013) Bile acids activate YAP to promote liver carcinogenesis. Cell Rep 5(4):1060–1069. 10.1016/j.celrep.2013.10.030. PMID:24268772
34. Varanasi SK, Chen D, Liu Y et al (2025) Bile acid synthesis impedes tumor-specific T cell responses during liver cancer. Science 387(6730):192–201. 10.1126/science.adl4100. PMID:39787217
35. Wei W, Zhang Z, Zhao X et al (2026) Bile acid retention impairs tumoral antigen presentation and intrinsic tumor suppression in MASH-HCC. Cancer Lett. ;654:218589. 10.1016/j.canlet.2026.218589. PMID:42173274
36. Wei H, Suo C, Gu X et al (2025) AKR1D1 suppresses liver cancer progression by promoting bile acid metabolism-mediated NK cell cytotoxicity. Cell Metab 37(5):1103–1118e7. 10.1016/j.cmet.2025.01.011. PMID:40010348

37. Meier PJ, Stieger B (2002) Bile salt transporters. Annu Rev Physiol 64:635–661. 10.1146/annurev.physiol.64.082201.100300. PMID:11826283
38. Goikoetxea-Usandizaga N, Serrano-Maciá M, Delgado TC et al (2022) Mitochondrial bioenergetics boost macrophage activation, promoting liver regeneration in metabolically compromised animals. Hepatology 75(3):550–566. 10.1002/hep.32149. PMID:34510498
39. Ma WK, Voss DM, Scharner J et al (2022) ASO-Based PKM Splice-Switching Therapy Inhibits Hepatocellular Carcinoma Growth. Cancer Res 82(5):900–915. 10.1158/0008-5472.CAN-20-0948. PMID:34921016
40. Chen L, Lin X, Lei Y et al (2022) Aerobic glycolysis enhances HBx-initiated hepatocellular carcinogenesis via NF-κBp65/HK2 signalling. J Exp Clin Cancer Res 41(1):329. 10.1186/s13046-022-02531-x. PMID:36411480
41. Shan Q, Yin L, Zhan Q et al (2024) The p-MYH9/USP22/HIF-1α axis promotes lenvatinib resistance and cancer stemness in hepatocellular carcinoma. Signal Transduct Target Ther 9(1):249. 10.1038/s41392-024-01963-5. PMID:39300073
42. Kim JE, Kim HS, Kim W et al (2025) Isoxazole-based molecules restore NK cell immune surveillance in hepatocarcinogenesis by targeting TM4SF5 and SLAMF7 linkage. Signal Transduct Target Ther 10(1):15. 10.1038/s41392-024-02106-6. PMID:39828766
43. Lu J, Chan TT, Wang Y et al (2025) FADD Activation in Hepatocellular Carcinoma Potentiates CD8 + T-cell Responses and Sensitizes to Immune Checkpoint Inhibitors. Cancer Res 85(18):3454–3470. 10.1158/0008-5472.CAN-24-3854. PMID:40658608
44. Thelen A, Scholz A, Benckert C et al (2008) VEGF-D promotes tumor growth and lymphatic spread in a mouse model of hepatocellular carcinoma. Int J Cancer 122(11):2471–2481. 10.1002/ijc.23439. PMID:18338756
45. Liu Y, Zhang JB, Qin Y et al (2013) PROX1 promotes hepatocellular carcinoma metastasis by way of up-regulating hypoxia-inducible factor 1α expression and protein stability. Hepatology 58(2):692–705. 10.1002/hep.26398. PMID:23505027
46. Li CZ, Ogawa H, Ng SS et al (2022) Human iPSC-derived hepatocyte system models cholestasis with tight junction protein 2 deficiency. JHEP Rep. ;4(4):100446. 10.1016/j.jhepr.2022.100446. PMID:35284810
47. Page MJ, McKenzie JE, Bossuyt PM et al (2021) The PRISMA 2020 statement: an updated guideline for reporting systematic reviews. BMJ 372:n71. 10.1136/bmj.n71. PMID:33782057
48. Villa E, Guido D, Critelli RM et al (2026) Large esophageal varices predict hepatocellular carcinoma in newly diagnosed cirrhosis: Insights from machine learning and propensity score analysis. Ann Hepatol. 10.1016/j.aohep.2026.102460. PMID:42860211
49. Benson AB 3rd, D'Angelica MI, Ahmed A et al (2026) NCCN Guidelines® Insights: Hepatocellular Carcinoma, Version 2.2026. J Natl Compr Canc Netw. 10.6004/jnccn.2026.0047. PMID:42874666
50. El-Serag HB, Thrift AP, Duong H et al (2024) Serum levels of total bile acids are associated with an increased risk of HCC in patients with cirrhosis. Hepatol Commun 8(11).

10.1097/HC9.0000000000000545. PMID:39652379

51. Dong TS, Jacobs JP, Agopian V et al (2022) Duodenal microbiome and serum metabolites predict hepatocellular carcinoma in a multicenter cohort of patients with cirrhosis. Dig Dis Sci 67(8):3831–3841. 10.1007/s10620-021-07299-2. PMID:34799768
52. Watling CZ, Petrick JL, Graubard BI et al (2025) Pre-diagnostic circulating bile acid concentrations and liver cancer risk: a nested case-control analysis of 12 cohorts. JNCI Cancer Spectr 9(5). 10.1093/jncics/pkaf086. PMID:40972035
53. Petrick JL, Florio AA, Koshiol J et al (2020) Prediagnostic concentrations of circulating bile acids and hepatocellular carcinoma risk: REVEAL-HBV and HCV studies. Int J Cancer 147(10):2743–2753. 10.1002/ijc.33051. PMID:32406072
54. Yu YC, Luu HN, Wang R et al (2022) Serum biomarkers of iron status and risk of hepatocellular carcinoma development in patients with nonalcoholic fatty liver disease. Cancer Epidemiol Biomarkers Prev 31(1):230–235. 10.1158/1055-9965.EPI-21-0754. PMID:34649958
55. Natarajan Y, Patel P, Chu J et al (2023) Risk of hepatocellular carcinoma in patients with various HFE genotypes. Dig Dis Sci 68(1):312–322. 10.1007/s10620-022-07602-9. PMID:35790703
56. Song BG, Goh MJ, Kang W et al (2025) Serum ferritin levels and liver-related events in individuals with steatotic liver disease: a longitudinal cohort study. Aliment Pharmacol Ther 61(3):491–500. 10.1111/apt.18402. PMID:39573902
57. Song Y, Chen H, Li J et al (2024) Lower serum albumin level: a prospective risk predictor of hepatocellular carcinoma in patients with chronic hepatitis B virus infection. J Viral Hepat 31(12):857–865. 10.1111/jvh.14008. PMID:39283028
58. Chon HY, Yim HJ, Heo SJ et al (2026) Enhanced prediction of hepatitis B virus-related hepatocellular carcinoma using age-male-albumin-bilirubin-platelet (aMAP) and liver stiffness assessed by vibration-controlled transient elastography. Clin Gastroenterol Hepatol 24(7):1897–1905. 10.1016/j.cgh.2025.09.039. PMID:41135666
59. Feng Z, Zhao H, Jiang Y et al (2020) Sarcopenia associates with increased risk of hepatocellular carcinoma among male patients with cirrhosis. Clin Nutr. ;39(10):3132–3139. 10.1016/j.clnu.2020.01.021. PMID:32057535
60. Li L, Hann HW, Wan S et al (2016) Cell-free circulating mitochondrial DNA content and risk of hepatocellular carcinoma in patients with chronic HBV infection. Sci Rep 6:23992. 10.1038/srep23992. PMID:27063412
61. Luo X, Yang W, Ma Y et al (2020) Physical activity and risk of hepatocellular carcinoma among U.S. men and women. Cancer Prev Res (Phila) 13(8):707–714. 10.1158/1940-6207.CAPR-19-0447. PMID:32312712
62. Lin ZZ, Xu YC, Liu CX et al (2021) Physical activity and liver cancer risk: a systematic review and meta-analyses. Clin J Sport Med 31(1):86–90. 10.1097/JSM.0000000000000689. PMID:30371534
63. Ganne-Carrié N, Layese R, Bourcier V et al (2016) Nomogram for individualized prediction of hepatocellular carcinoma occurrence in hepatitis C virus cirrhosis (ANRS CO12 CirVir). Hepatology

64(4):1136–1147. 10.1002/hep.28702. PMID:27348075

64. Stepien M, Fedirko V, Duarte-Salles T et al (2016) Prospective association of liver function biomarkers with development of hepatobiliary cancers. Cancer Epidemiol 40:179–187. 10.1016/j.canep.2016.01.002. PMID:26773278
65. Fan R, Papatheodoridis G, Sun J et al (2020) aMAP risk score predicts hepatocellular carcinoma development in patients with chronic hepatitis. J Hepatol 73(6):1368–1378. 10.1016/j.jhep.2020.07.025. PMID:32707225
66. Fujiwara N, Lopez C, Marsh TL et al (2025) Phase 3 validation of PAaM for hepatocellular carcinoma risk stratification in cirrhosis. Gastroenterology 168(3):556–567e7. 10.1053/j.gastro.2024.10.035. PMID:39521255
67. Tseng CH (2018) Metformin and risk of hepatocellular carcinoma in patients with type 2 diabetes. Liver Int 38(11):2018–2027. 10.1111/liv.13872. PMID:29956875
68. Wang L, Berger NA, Kaelber DC et al (2024) Association of GLP-1 receptor agonists and hepatocellular carcinoma incidence and hepatic decompensation in patients with type 2 diabetes. Gastroenterology 167(4):689–703. 10.1053/j.gastro.2024.04.029. PMID:38692395
69. Wong YJ, Qiu TY, Ng GK et al (2021) Efficacy and safety of statin for hepatocellular carcinoma prevention among chronic liver disease patients: a systematic review and meta-analysis. J Clin Gastroenterol 55(7):615–623. 10.1097/MCG.0000000000001478. PMID:33606427
70. He X, Zhao Z, Jiang X et al (2023) Non-selective beta-blockers and the incidence of hepatocellular carcinoma in patients with cirrhosis: a meta-analysis. Front Pharmacol. ;14:1216059. 10.3389/fphar.2023.1216059. PMID:37538177
71. Yeoh BS, Saha P, Golonka RM et al (2022) Enterohepatic shunt-driven cholemia predisposes to liver cancer. Gastroenterology 163(6):1658–1671e16. 10.1053/j.gastro.2022.08.033. PMID:35988658
72. Roberts KJ, Bannister CA, Schrem H et al (2019) Enzyme replacement improves survival among patients with pancreatic cancer: results of a population based study. Pancreatology 19(1):114–121. 10.1016/j.pan.2018.10.010. PMID:30385188
73. Dugic A, Hagström H et al (2026) Association between pancreatic enzyme replacement therapy and mortality in pancreatic cancer: a matched case-control study. Pancreatology. ;26(1):130–137. 10.1016/j.pan.2025.12.008. PMID:41387158

Figures

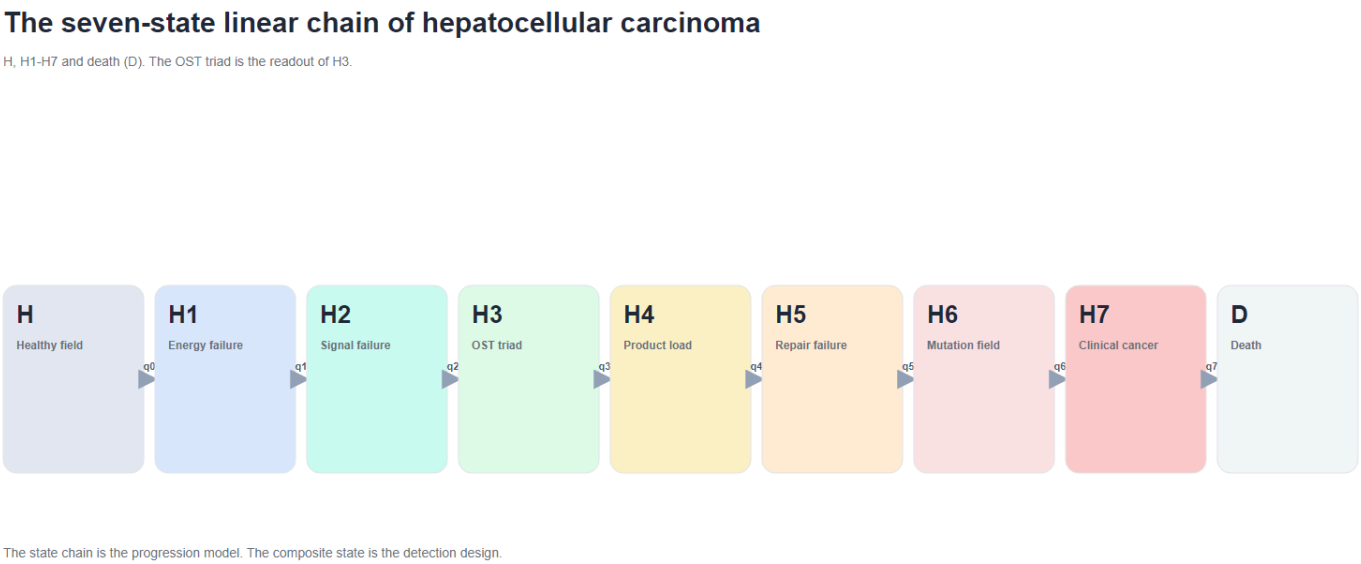


Figure 1

The seven-state linear chain of hepatocellular carcinoma. H, H1-H7 and death (D). The OST triad is the readout of H3; the six product groups are the readout of H4.

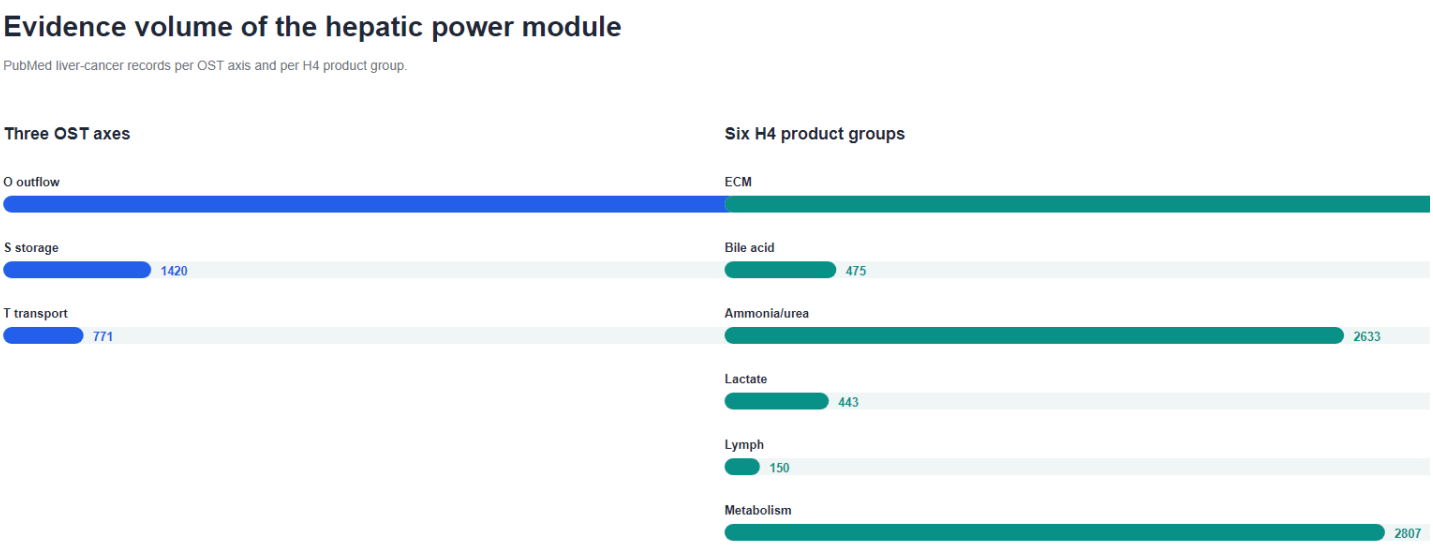


Figure 2

Evidence volume by axis and product group. PubMed liver-cancer records for the three OST axes and the six H4 product groups.

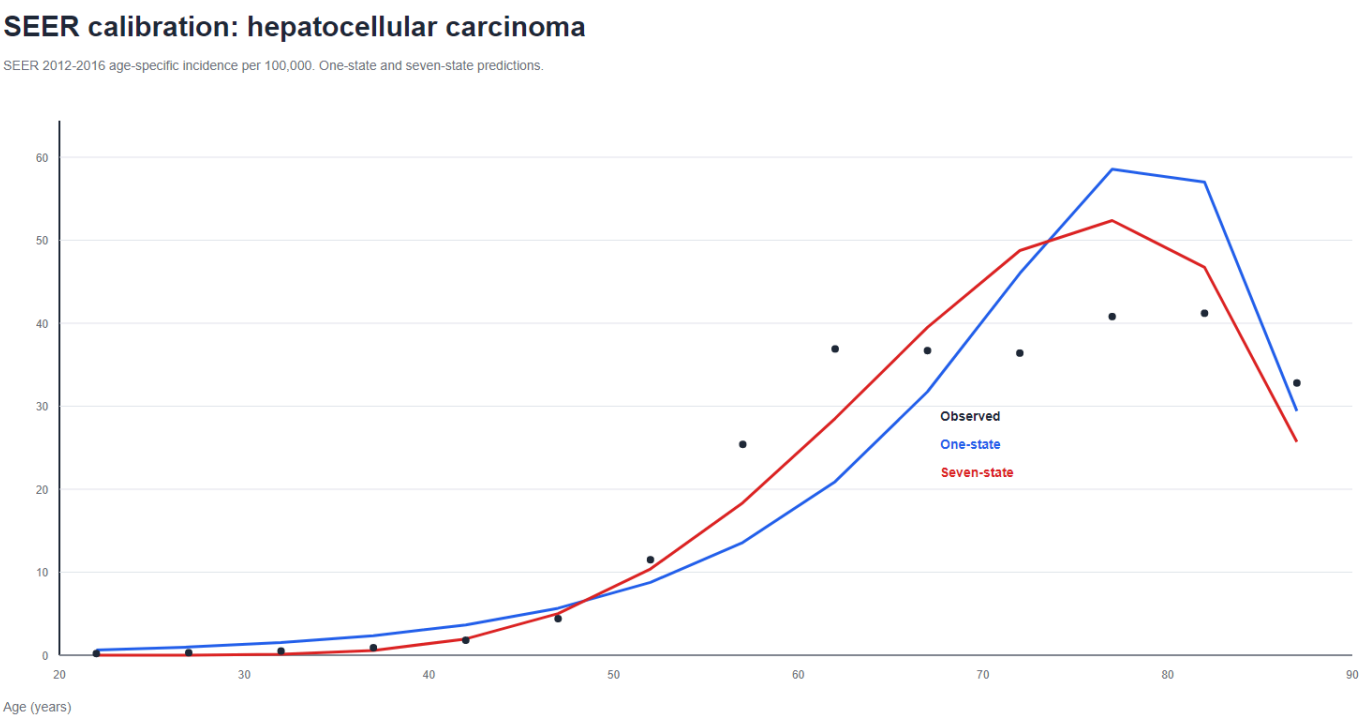


Figure 3

Calibration against SEER age-specific incidence. Observed and predicted age-specific incidence. The one-state model tracks the aggregate curve; the seven-state model fits the middle.

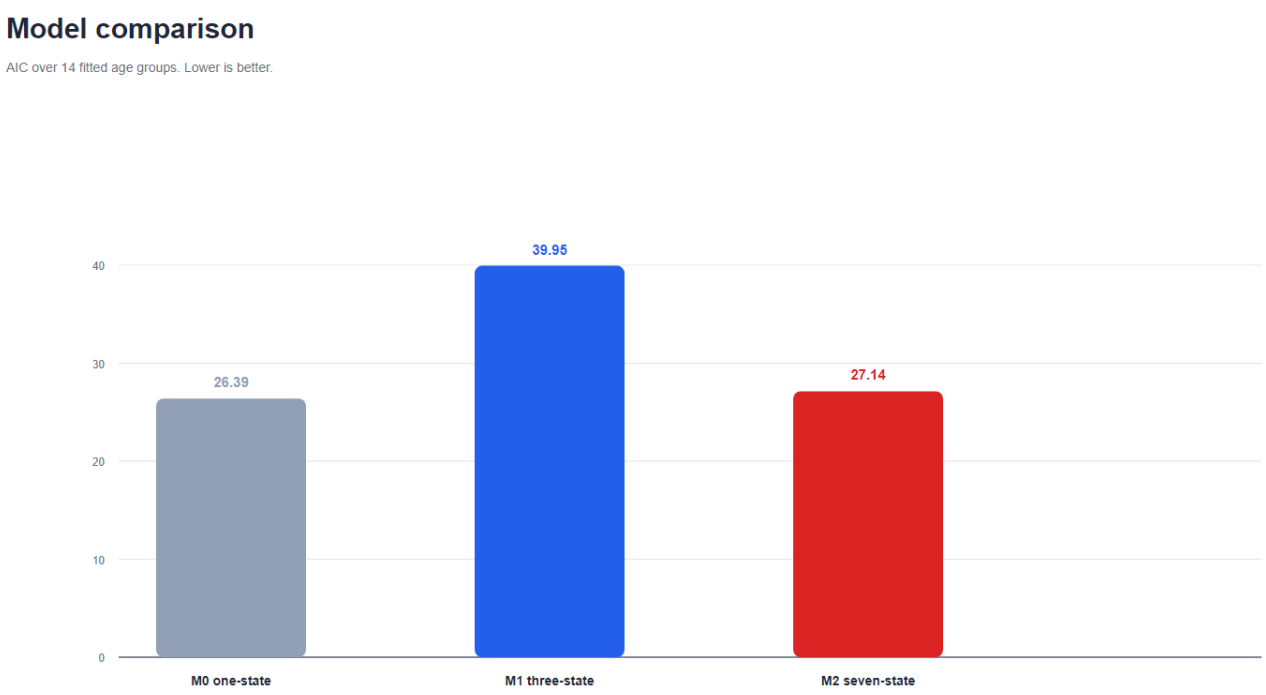


Figure 4

Model comparison. AIC and BIC for the one-state, three-state and seven-state models. The four intermediate rates collapse to one value.

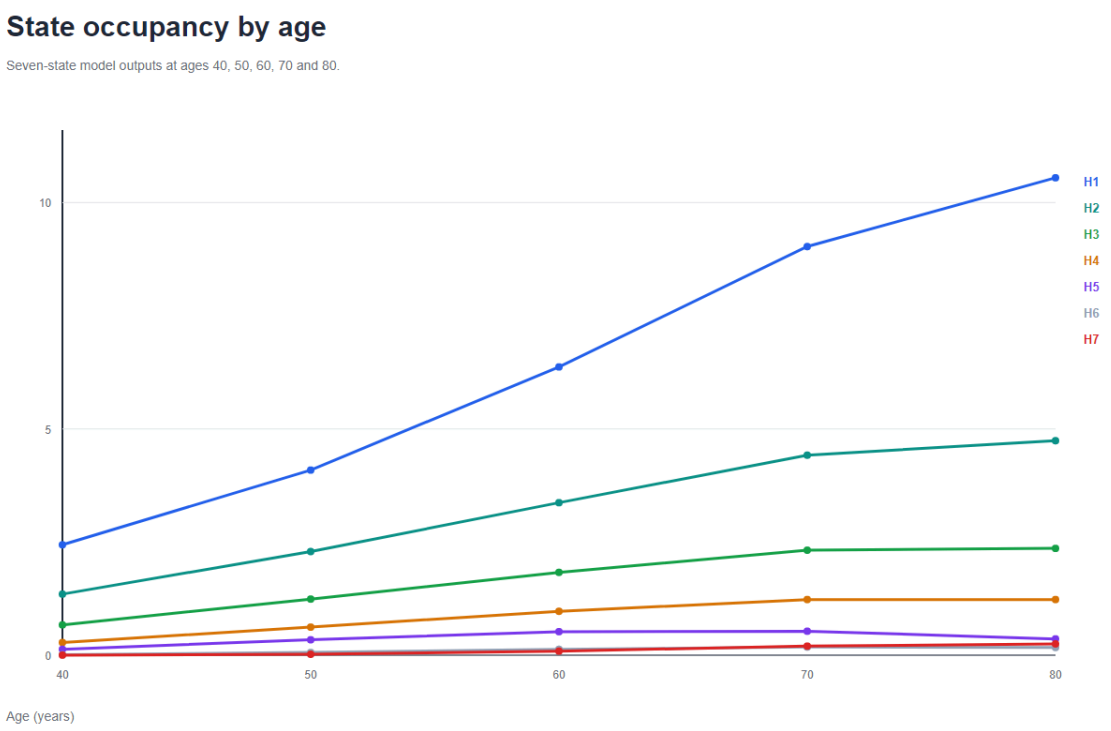


Figure 5

State occupancy by age. H1-H7 occupancy at ages 40, 50, 60, 70 and 80.

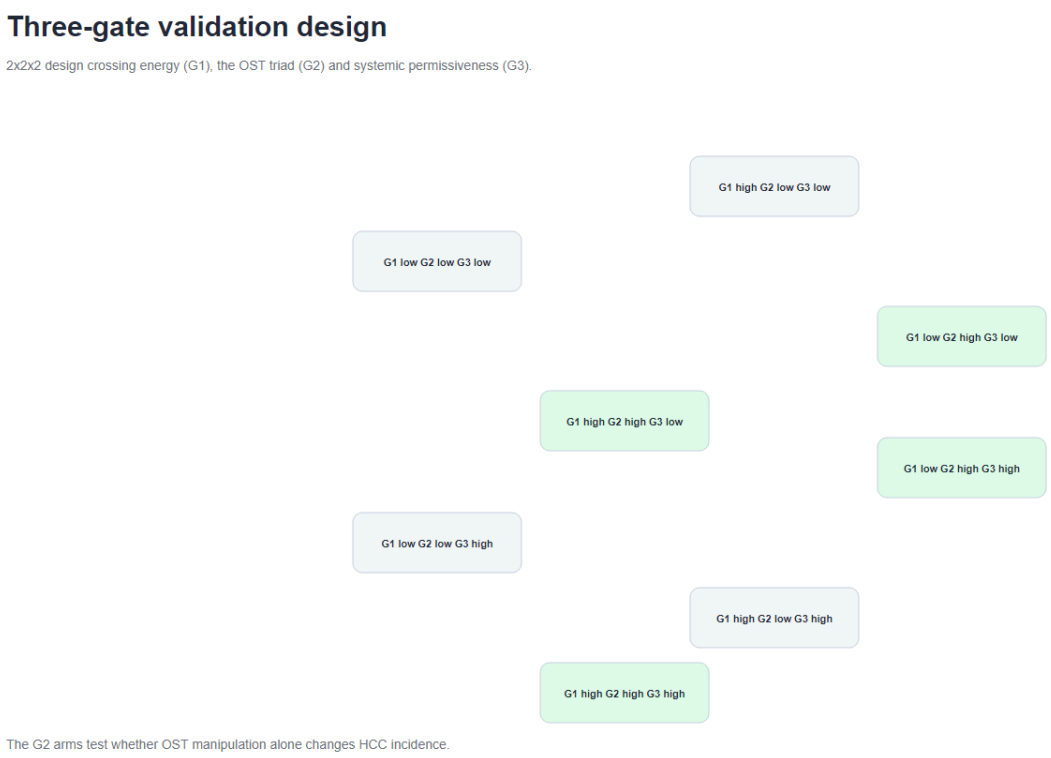


Figure 6

The three-gate validation design. 2x2x2 design crossing energy, the OST triad and systemic permissiveness. The G2 arms test whether OST manipulation alone changes HCC incidence.

Supplementary Files

This is a list of supplementary files associated with this preprint. Click to download.

- SupplementaryTablesS1S7.docx